JOURNAL OF GEOPHYSICAL RESEARCH, VOL. 111, A06107, doi:10.1029/2005JA011431, 2006

Are halo coronal mass ejections special events?

Alejandro Lara,[1] Nat Gopalswamy,[2] Hong Xie,[3] Eduardo Mendoza-Torres,[4] Román Pérez-Eríquez,[5] and Gregory Michalek[6]

Received 18 September 2005; revised 13 March 2006; accepted 17 March 2006; published 22 June 2006.

[1] We revisited the properties of wide coronal mass ejections (CMEs) called halo CMEs. Using the large LASCO/SOHO CMEs data set, from 1996 to 2004, we examined the statistical properties of (partial and full) halo CMEs and compare with the same properties of "normal" width (lower than 120°) CMEs. We found that halo CMEs have different properties than "normal" CMEs, which cannot be explained merely by the current geometric interpretation that they are seen as halos because they are traveling in the Sun Earth direction. We found that the CME width distribution is formed by, at least, three different populations: Two gaussians: a narrow and a medium distribution centered at ∼17° and ∼38°, respectively; the narrow population most likely corresponds to the "true" observed widths, whereas the medium width population is the product of projection effects. The third distribution corresponds to wider CMEs ($80° < W < 210°$) which behaves as a power law. Partial and full halo CMEs wider than these do not follow any particular distribution. This lack of regularity may be due to the small number of such events. In particular, we found (and test by a statistical approach) that the number of observed full halo CMEs is lower than expected. The CME speed follows a log-normal distribution, except for the very low speed CME population, which follows a gaussian distribution centered at ∼100 km/s and is probably due to projection effects. When the CMEs are divided by width into nonhalo, partial halo, and full halo, we found that the peaks of the distributions are shifted toward higher speeds, ∼300, ∼400 and ∼600 km/s for nonhalo, partial halo, and full halo CMEs, respectively. This confirms that halo CMEs tend to be high speed CMEs. The acceleration of full halo CMEs tends to be more negative compared with nonhalo and partial halo CMEs. We introduce a new observational CME parameter: The final observed distance (FOD), i.e., the highest point within the coronograph field of view where a CME can be distinguished from the background. In other words, the highest CME altitude measured. The FOD for nonhalo CMEs decreases exponentially from ∼5 to ∼30 $R_\odot$ in the LASCO field of view. On the other hand, the FOD of halo CMEs increase with distance. This means that it is more likely to see halo CMEs at large distances (from the Sun) than nonhalo CMEs. These halo CME properties may be explained if the white light wide enhancements (or halo) seen by coronographs correspond to a combination of an expanding (shock) wave which disturbs and/or compresses the ambient material and the CME material itself.

Citation: Lara, A., N. Gopalswamy, H. Xie, E. Mendoza-Torres, R. Pérez-Eríquez, and G. Michalek (2006), Are halo coronal mass ejections special events?, *J. Geophys. Res.*, *111*, A06107, doi:10.1029/2005JA011431.

1. Introduction

[2] Coronal mass ejections (CMEs) are structures moving outward from the low corona to the interplanetary medium, commonly seen in white light by coronographs. The white light properties of CMEs have been studied extensively since their discovery in the 1970s [*Howard et al.*, 1985; *Hundhausen*, 1993; *Webb and Howard*, 1994; *St. Cyr et al.*, 2000; *Yashiro et al.*, 2004; *Gopalswamy*, 2004]. The main CME characteristics measured and reported are the speed, acceleration, position angle, and width. However, owing to an instrumental limitation, all of these parameters suffer from projection effects, i.e., we do not know the "real"

[1]Instituto de Geofísica, Universidad Nacional Autónoma de México, Mexico D. F., Mexico.
[2]NASA Goddard Space Flight Center, Greenbelt, Maryland, USA.
[3]Catholic University of America, Washington, DC, USA.
[4]Instituto Nacional De Astrofísica Óptica y Electrónica, Tonantzintla, Mexico.
[5]Centro de Geociencias, Universidad Nacional Autónoma de México, Juriquilla, Mexico.
[6]Astronomical Observatory of Jagiellonian University, Krakow, Poland.

0148-0227/06/2005JA011431$09.00

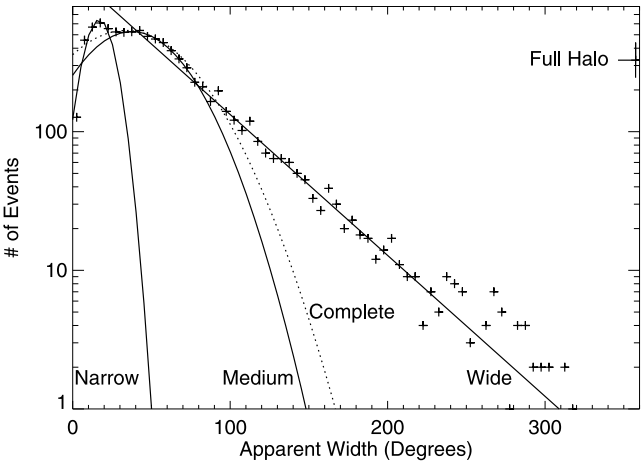

Figure 1. Observed CME width distribution (plus symbols) in a bin size of 5°. Continuous lines represent models fitted to the points in different width intervals. The dotted line is the gaussian model fitted to the entire width range. The big plus symbol at 360° indicates the number of full halo CMEs.

(three-dimensional) value of these parameters, but only the projection in the plane of the sky (POS). The CME width is not only affected by such projection effects but is also affected by the sensibility of the instrument. For example, from Skylab observations it was not clear whether CMEs had a three dimensional structure [*Crifo et al.*, 1983] or coplanar loop-like structures [*Trottet and McQueen*, 1980]. This ambiguity was solved by the Solwind coronograph observation of an Earth directed CME reported by *Howard et al.* [1982]. These authors used the term "halo" for this kind of events and interpreted it as "regular" wide CMEs traveling in the Sun-observer direction (toward or away), and originated from the near center of the disk. Recently, *St. Cyr et al.* [2005] divided wide CMEs in three categories: The first one corresponds to the original [*Howard et al.*, 1982] interpretation; In the second one, the halo is interpreted as a (shock) wave created by the eruption, traveling through the corona and deflecting the streamers, so that it is seen as a wide perturbation [*Hundhausen*, 1987; *Sime and Hundhausen*, 1987; *Sheeley et al.*, 2000]; The third category consists of multiple CMEs erupted at (almost) the same time and appearing as a single wide structure to the observer. *St. Cyr et al.* [2005] states that any of these three possibilities may be seen with coronographs (although the first one is the more generally accepted nowadays). From an observational point of view, wide CMEs are categorized as partial and full halo, depending on their width, in this work we use this convention and will refer as nonhalo, partial halo, and full halo to CMEs with width lower than 120°, between 120° and 320° and greater than 320°, respectively.

[3] In terms of space weather, halo CMEs are the most important due to the fact that they are most likely to reach the Earth (at least half of them) and tend to be more geoeffective. However, the relationship is not one to one, i.e., there are halo CMEs without signatures in the near Earth space [*St. Cyr et al.*, 2000; *Wang et al.*, 2002] and there are strong geomagnetic storms without a clear unique associated halo CME [*Zhang et al.*, 2003].

[4] The Large Angle and Spectrometric Coronagraph's (LASCO) [*Brueckner et al.*, 1995] sensitivity is much higher than previous coronographs [*St. Cyr et al.*, 2000]; in particular, LASCO observed more than 9000 CMEs during the 1996–2004 period. Thus it is expected that any statistical result obtained from this database may have a higher degree of confidence. In this work we present a statistical analysis of the common CME parameters as width (section 2.1), speed (section 2.2), acceleration (section 2.3), and position angle (section 2.4). We introduce a new CME parameter, the final observed distance (FOD), as the last point in the LASCO field of view, where the CME enhancement is distinguishable from the background level and we discuss the FOD statistical behavior (section 3). In general, we found that the properties of halo CMEs are statistically different from those for narrow CMEs, suggesting that they are different phenomena. We propose a possible scenario to explain such differences. In this scenario, the observed halo is a combination of the enhancement produced by the shock (driven by a fast CME) plus the CME material (section 4).

2. Statistical Results

2.1. Width

[5] The width is measured as the angle subtended by the lateral borders of the CME with vertex at the center of the disk. There may be minor errors on the width measurement. For example, it is possible to include changes in the background coronal structures as part of the CME, increasing the measured width by few degrees. This problem is present only in few weak events and do not changes appreciably the CME width distribution. Figure 1 shows the distribution of the apparent widths (plus symbols) of 9224 CMEs observed by LASCO (and cataloged at http://cdaw.gsfc.nasa.gov) from 1996 to 2004. The distribution bin size is 5° and the large plus symbol at 360° represents the number of full halo CMEs.

[6] The distribution shows various modes, and is not well fitted by a single function as shown in Figure 1 where we have plotted (dotted line) the fitted gaussian to the entire distribution (from 0° to 360°). When we divided the distribution in different width intervals, the fitting process is better (it is difficult to compare the goodness of fit because we are fitting in different data intervals). For narrow widths ($W_N < 25°$), a gaussian model can be fitted:

$$f(W_N) = 642.5 \exp\left(-\frac{1}{2}\left(\frac{W_N - 16.8}{9.3}\right)^2\right). \quad (1)$$

For the 30°–80° medium width (W_M) interval, again a gaussian model fits very well the distribution

$$f(W_M) = 527.7 \exp\left(-\frac{1}{2}\left(\frac{W_M - 37.6}{31.2}\right)^2\right). \quad (2)$$

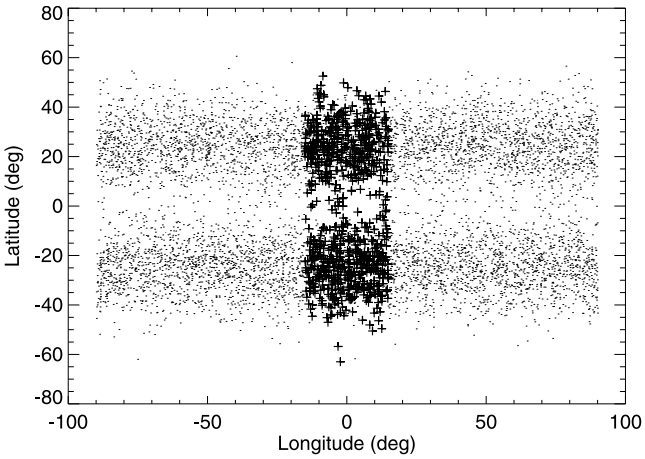

Figure 2. Dots represent the positions in heliocoordinates of the randomly created CME sequence. Plus symbols mark the position of the CMEs close to the center of the disk, which have an angular width larger than 30° and should be seen as full halo CMEs by coronographs similar to LASCO.

After this, in the 80°–210° interval, the number of CMEs with large widths (W_L), decrease exponentially following the relation:

$$f(W_L) = 1381.8 \exp(-0.023 W_L). \quad (3)$$

Above ~210° the dispersion is very high and the distribution no longer follows the exponential function. Therefore, these "widest" events are not part of the same distribution. Models described by equations (1), (2), and (3) are plotted in continuous lines (marked as narrow, medium and wide, respectively) in Figure 1.

[7] The mean width of the entire distribution ($W \leq 360°$), is ~67°, similar to the 72° found by *St. Cyr et al.* [2000]. The mean width of nonhalo CMEs ($W \leq 120°$) is ~46°, again close to previous reported values (for example, 47° in the work of *St. Cyr et al.* [2000] and 47°–61° in the work of *Yashiro et al.* [2004]). These values may be compared with the values found by *Hundhausen* [1993] with CMEs observed by lower sensitivity coronographs, Skylab (42°) and SMM (47°). In such previous works, the width was analyzed as a single (gaussian) distribution. On the other hand, in this work, the large data base allows us to perform a more detailed statistical analysis by dividing the distribution in different width intervals.

[8] It is interesting to note that the percentage of events in the narrow, medium and large width intervals are 25.1%, 45.6% and 19.0%, respectively. Thus only ~10% of the events seem to be in the widest part of the distribution. In particular, the number of full halo CMEs is 328 (3.5%). This number is somewhat less than expected, as shown by the following simple analysis, where we assume that all CMEs with width larger than 30° coming from the center of the disk should be seen as full halos.

2.2. Number of Full Halo CMEs

[9] As a first approximation we can consider a conical CME expansion, with an opening angle of 30° and vertex at the Sun center. The cone cross section at a radial distance of ~4.6 (8.3) $R_\odot$ from the surface, is 3 (5) $R_\odot$. This cross section is larger than the C2 (C3) occulter ~2 (4) $R_\odot$, and then, if this CME is lunched close to the disk center, it should be seen as a halo CME. The number of events with apparent width larger than 30° is 6481. Thus, dividing the solar longitude in sectors of 30° and assuming the same CME eruption probability for each sector, we can expect about 540 events coming from the −15° to 15° heliolongitude range, i.e., from the region close to the center of the disk; and a similar number from its antipode region. Such events have enough width to be seen as full halos in the LASCO field of view and correspond to 5.8% of the total number of CMEs, almost two times the observed number. The lack of halo CMEs number suggest that the geometrical interpretation is not enough to explain the observations.

[10] In order to confirm the previous analysis about the low number of observed halo CMEs, we create a random sequence of CMEs under the following conditions: (1) The CME width (W) follows the medium width gaussian model (equation (2)) which represent ~50% of the CME population; (2) The CME longitude (ϕ) is uniformly distributed from E90 to W90 and (3) The CME latitude (λ) is normally distributed in two bands of $\sigma = 20°$ around the N25 and S25 parallels (*Wang et al.* [2002] studied 132 front side halo CMEs and the location of the associated event in the disk and they found that ~78% of such events took place inside the ±10°–30° latitude bands). The latitude and longitude of each CME is represented with a dot in Figure 2. The distribution of the random sequence of CMEs is shown as a continuous line in Figure 3. Counting the number of events which falls in the −15° to 15° heliolongitude range and have width larger than 30° (marked as plus symbols in Figure 2), we can get an idea of the most probable rate of halo CMEs. Running this simple approximation several times to assure stability (100 runs) and averaging the results, we obtained a total of 7382 CMEs with width larger than 5° (our imposed lower limit). From this number we have 394 and 831 CMEs in the center of the disk region (±15° of longitude) which have a width lower and larger than 30°, respectively. Assuming that CMEs with widths lower than

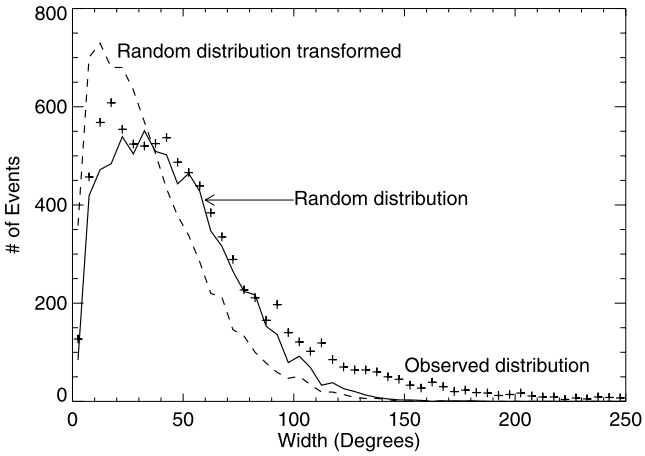

Figure 3. Width distribution of the randomly created CME sequence (continuous line) and its geometrical transformation (dashed line). In order to compare, plus symbols denote the observed width distribution.

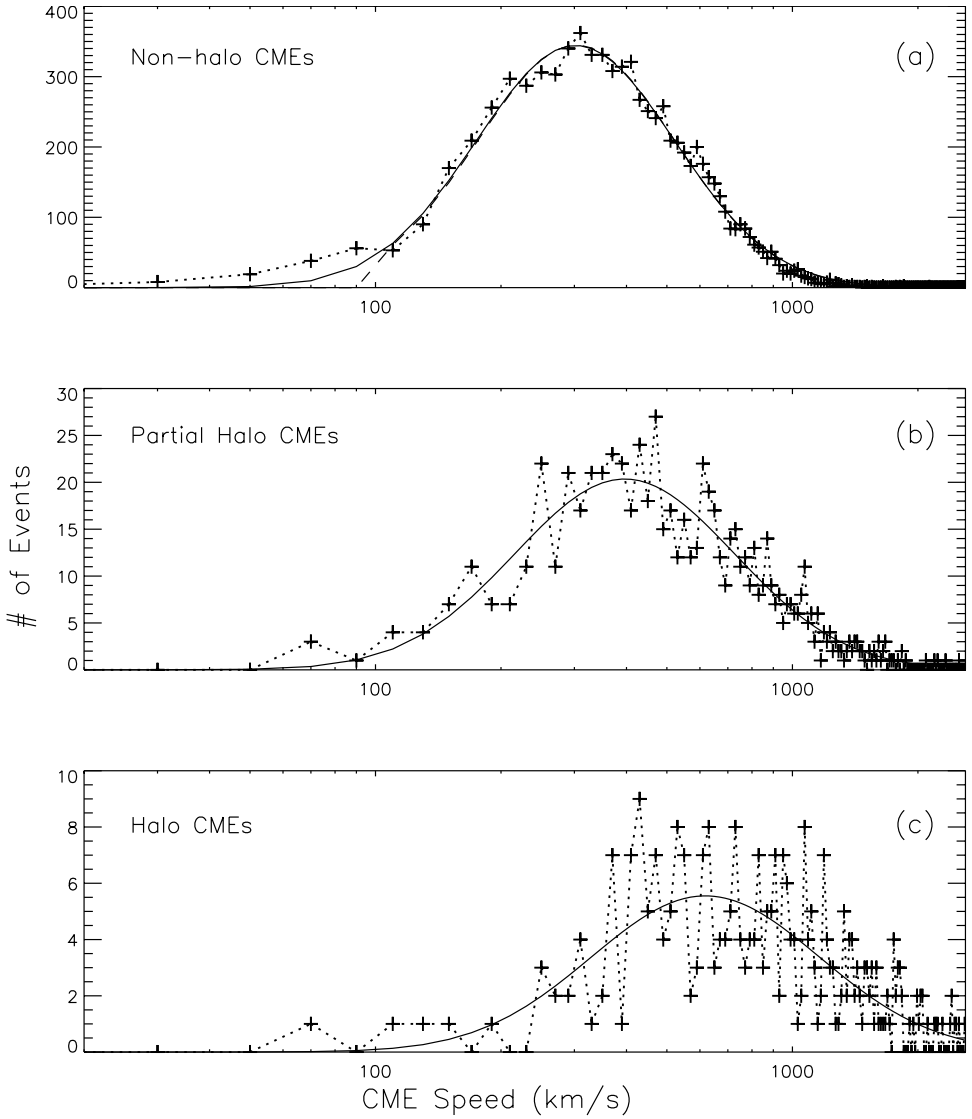

Figure 4. Plus symbols mark the observed CME speed distributions in bin sizes of 20 km/s. From top to bottom panels are the no, partial and full halo speed distributions. The curves are the distribution models fitted to the points.

30° cannot be seen by the coronographs, we may speculate that ∼5.3% of central CMEs are missed by such instruments. On the other hand, we should observe ∼11.9% of the total number as full halo CMEs. These numbers are the minima quotes, as the imposed limits for full halos are very conservative. For instance, *Wang et al.* [2002] found that ∼83% of front side halo CMEs have associated surface locations within ±30° of center meridian. By extending the longitude range and/or lowering the CME width limit, the percentage of full halos CMEs increases considerably. For instance, we should observe 17% of full halo CMEs when the width limit is 20° and the longitude range is ±20°.

[11] An obvious problem of the previous analysis is that we are using the projected widths, so the results are biased toward larger widths (due to the projection) so that we have a larger number of expected full halo CMEs. To avoid this problem we can deproject the random distribution and perform the same analysis to the deprojected random CME set. Once we know the apparent width and the center position of a CME projection on POS, it is possible to apply a geometric coordinate transformation to obtain the real (with no projection effects) CME width. We apply the following transformation to the random CME distribution.

$$\theta = \tan^{-1}\frac{\cos\lambda\cos\phi}{\sqrt{(\cos\lambda\sin\phi)^2+\sin^2\phi}}$$
$$W_0/2 = \tan^{-1}(b/h)$$
$$W_r/2 = \tan^{-1}(\tan(W_0/2)\cos\theta) \quad (4)$$

where W_0 and W_r are the apparent and transformed (real) widths, respectively. b and h are the CME projection major axis and the center displacement on POS. λ and ϕ are the latitude and longitude angles relative to the ecliptic plane in the heliospheric coordinate system; and θ is the angle between the central axis of a CME and POS (see *Xie et al.*

Table 1. Coefficients of Speed Distributions

CME	Coefficients		
Halo	α	μ	σ
Nonhalo	343.9	5.7	0.5
Nonhalo$_{v>100}$	344.4	5.7	0.5
Partial halo	20.1	6.0	0.6
Full halo	5.8	6.4	0.6

[2004] for details). The transformed distribution is plotted with a dash line in Figure 3. As expected, the transformed distribution is shifted towards lower widths and resembles very well the narrow width distribution. From this, we may conclude that the double gaussian shape at narrow and medium widths of the observed widths is the result of projection effects, i.e., is the superposition of the true (narrow) and projected (medium) width distributions (a detailed discussion of this subject is under preparation and will be published elsewhere).

[12] Performing the same analysis about the number of halo CMEs but now using the transformed distribution, we get 898 and 327 CMEs with width lower and higher than 30°, respectively, from a total of 7382. In this case, we are missing 12% of center CMEs and we should expect 4.4% of halo CMEs. As this is a minimum limit, this percentage is still higher than the 3.5% observed.

2.3. Speed

[13] The CME speed is computed by measuring the distance, to the center of the disk, of the CME leading edge (projected on POS) for all frames of LASCO observations where the CME is visible. The time of each frame is known and then the speed can be easily obtained.

[14] Plus symbols in Figure 4, joined by a dotted line, show the observed CME speed distributions for different widths. The distributions are of the so called "log-normal" type and the continuous lines are the fitted gaussians obtained with the transformation $v' = \ln(v)$. The bin size for all cases is 20 km/s. The fitted distributions are of the form

$$f(v) = \alpha \exp\left(-\frac{1}{2}\left(\frac{\ln(v)-\mu}{\sigma}\right)^2\right), \quad (5)$$

and the α, μ and σ coefficients for all cases are shown in Table 1 (first row for nonhalo CMEs). Nonhalo CMEs (width <120°) are plotted in Figure 4a. In this case, the distribution peaks at 302.0 km/s. Note that at speeds lower than 100 km/s, the distribution changes significantly. Thus in order to analyze this change, we divided the nonhalo CMEs into two speed intervals, lower and higher than 100 km/s. The distribution for nonhalo CMEs with a speed higher than 100 km/s is almost the same as the previous one (equation (5)) and the coefficients are listed in the second row of Table 1. In this case the distribution peak value is 303.2 km/s, and is plotted as a dashed line in Figure 4a.

[15] The distribution of CMEs with speeds lower than 100 km/s is completely different. It is well fitted by the gaussian function

$$f(v) = 56.3 \exp\left(-\frac{1}{2}\left(\frac{v-92.2}{29.5}\right)^2\right) \quad (6)$$

This imply that very low speed CME are not part of regular CMEs. This deviation may be due, for instance, to projection effects.

[16] The central panel in Figure 4 shows the speed distribution for partial halo CMEs. The distribution is of the form of equation (5) with the coefficients given in the third row of Table 1. The distribution peaks at 392.0 km/s. The dispersion is high due to the lower number of events (the problem is worst for full halo CMEs). The distribution of full halo CMEs is plotted in Figure 4c. In this case the fitted coefficients are shown in the fourth row of Table 1, and the peak is at 615.5 km/s.

[17] The distributions of nonhalo, partial halo, and full halo CME speeds are similar, but clearly shifted toward higher speeds, nonhalo CMEs peaks at lower speed, whereas halo CMEs distribution peaks at higher speeds. This is a confirmation of previous results where the average speed of halo CMEs has been reported as higher than the average speed of normal CMEs [*Yashiro et al.*, 2004; *Gopalswamy*, 2004].

[18] By adding all contributions to the speed distribution, we are able to obtain a good approximation to the total CME speed distribution. This is shown in Figure 5 where, again, plus symbols denote the observed total CME speed distribution, and the distributions discussed above are plotted as: (1) a dotted line is the gaussian distribution for all CMEs with speed lower than 100 km/s; (2) a dot-dash line is the distribution for non-halo CMEs with speed higher than 100 km/s; (3) a three-dot-dash line is the speed distribution of partial halo CMEs; (4) a dashed line is the speed distribution of full halo CMEs (for clarity, the later two distributions (partial and full halo CMEs) are multiplied by a factor of ten); (5) and the continuous line is the addition of all distributions and fits very well the observed data.

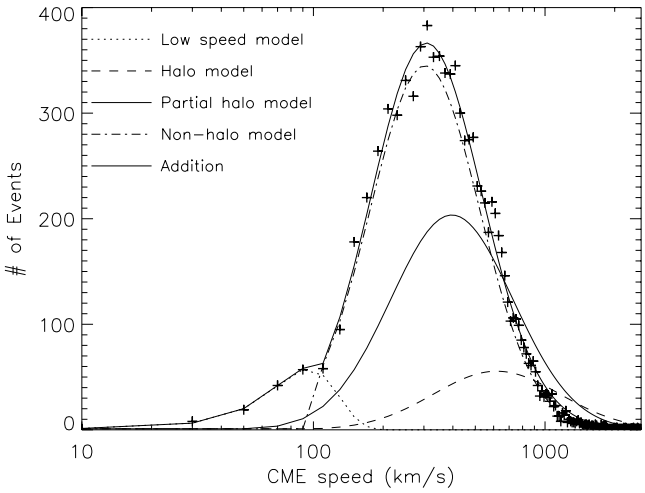

Figure 5. The observed CME speed distribution (plus symbols); the gaussian model for low speeds (dotted line); the log-normal models for nonhalo (dot-dash), partial halo (three dot-dash), and full halo (dash) CMEs. For clarity, the last two models are multiplied by a factor of ten. The addition of all models is plotted in continuous line.

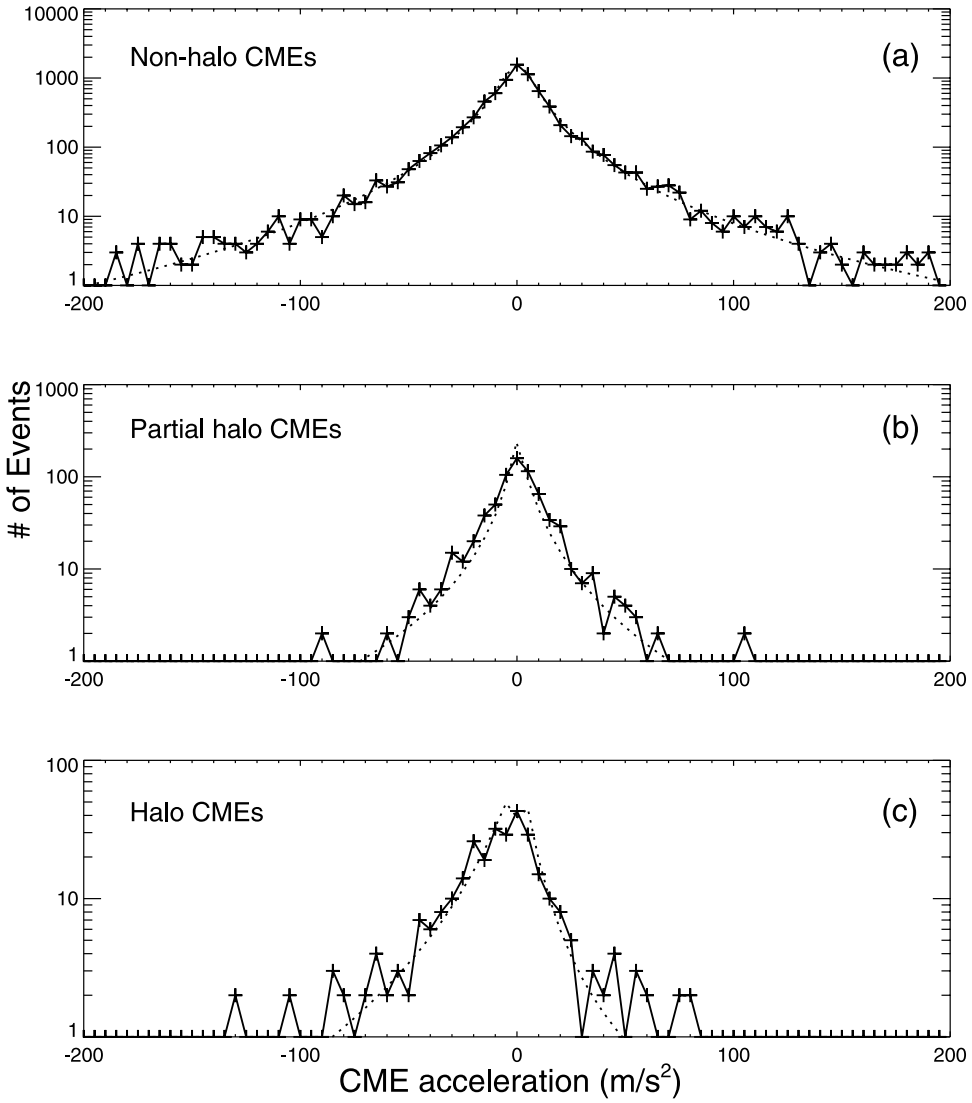

Figure 6. Acceleration distributions for nonhalo (top), partial halo (middle), and full halo (bottom) CMEs, the bin size is 5 m/s^2, and the central bin includes zero acceleration.

2.4. Acceleration

[19] The acceleration distribution is less regular, it does not seems to follow any standard distribution function, and thus is difficult to obtain quantitative information. Figure 6 shows the observed CME acceleration distribution for nonhalos (Figure 6a), partial halos (Figure 6b), and full halos (Figure 6c). There is no a clear difference between nonhalo and partial halo acceleration distributions, although, the acceleration distribution for halo CMEs shows a clear tendency toward negative values. The bin size is 5 m/s^2 and we include zero acceleration in the central bin (from -2.5 to 2.5 m/s^2), 28.8%, 23.6%, and 19.8% of events fall in this $\sim$zero acceleration bin, for nonhalo, partial halo, and full halo CMEs, respectively. 35.7%, 39.7%, and 27.0% of the events are on the positive side of the distribution; whereas 35.4%, 36.7%, and 52.8% are on the negative side, for nonhalo, partial halo, and full halo, respectively. The number of full halo CMEs with negative acceleration is clearly higher than the number of zero and positive acceleration full halo CMEs. Commonly, halo CMEs show deceleration [*Sheeley et al.*, 1999; *Yashiro et al.*, 2004; *Gopalswamy*, 2004], in particular, *Gopalswamy et al.* [2001b] interpreted the fast speed CME deceleration as a result of the drag force which is proportional to speed. However, *Sheeley et al.* [1999] suggested that the observed deceleration "might be caused by shock waves sweeping up material far from the Sun."

2.5. Position Angle

[20] The position angle (PA) is the angle of the axis of the CME projected cone, measured counterclockwise from solar north [*Hundhausen*, 1993]. For halo CMEs the PA is the angle where the speed is computed and corresponds to the PA of the brightest structure of the leading edge. The PA circular distributions are presented in Figures 7 and 8, where the symbols represent the normalized number of events in an angular bin of 5°. For clarity, we added a constant value of 0.01 to the distributions, in such a way that zero level is marked by a dotted line in these figures.

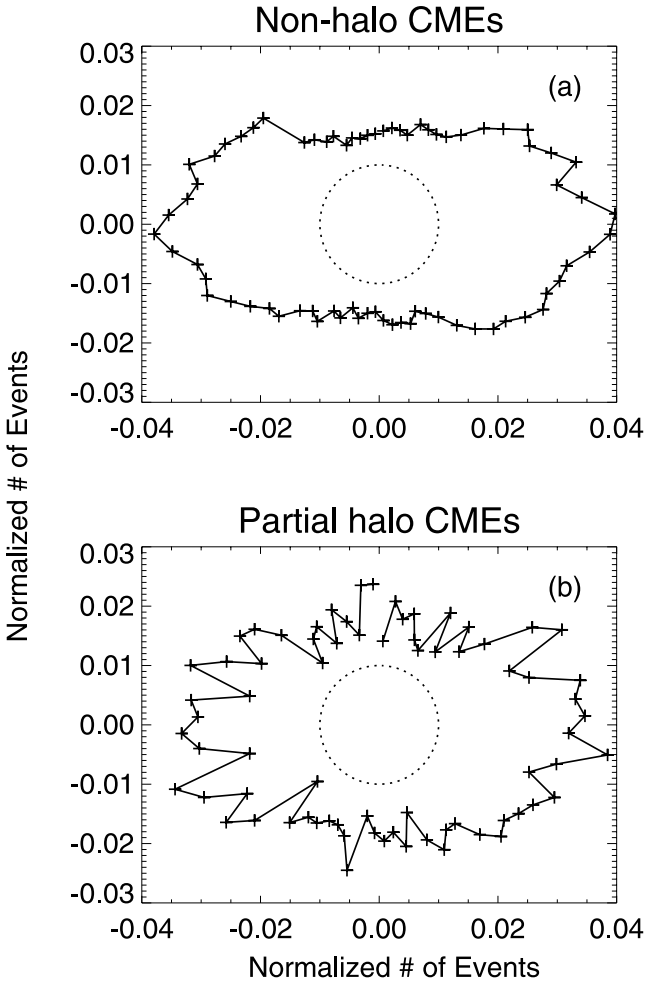

Figure 7. Normalized PA circular distribution for nonhalo (top) and partial halo (bottom) CMEs. The bin size is 5° and, for clarity, we added a constant value of 0.01 to the distribution (dotted line).

[21] The PA distribution for nonhalo CMEs is shown in Figure 7a. Clearly, the distribution peaks at equatorial latitudes, even though it shows a small asymmetry. In order to quantify this asymmetry, Table 2 shows the percentage of events in each quadrant. Northeast (NE), southeast (SE), southwest (SW), and northwest (NW) are in columns 2 to 5, respectively, for nonhalo, partial halo, and full halo CMEs in rows 1 to 3, respectively. The east-west asymmetry is small but appreciable with 52.5%, 51.3%, and 51.9% of nonhalo, partial, and full halo events falling in the western hemisphere, The SW quadrant seems to have the greatest number of CMEs. A chi-squared test gives a a probability lower than 0.001 of getting these percentages by chance assuming either of the two null hypothesis: (1) an equal probability (0.25) to erupt CMEs in each quadrant or (2) taking into account the occulter pylon and giving a lower probability (0.23 as instance) to the SE quadrant.

2.6. Final Observed Distance

[22] Inside the field of view of LASCO, there is a limit distance where the CME brightness excess reach the background brightness level. At this point the observer can no longer follow the CME leading edge. We call this limit distance the final observation distance (FOD). The total CME FOD distribution is plotted in Figure 9a. The FOD distribution follows an exponential law from 5 to ~21 $R_\odot$. Above this height, the FOD distribution changes dramatically, the decreasing trend is inverted, implying that more CMEs are present at distances higher than ~21 $R_\odot$, than expected from the distribution trend.

[23] The number of observed CMEs (N) changes with distance (h) with the exponential law,

$$N = \delta \exp(\epsilon h), \tag{7}$$

where δ and ϵ are constants (see Table 3). This function is shown by the continuous line in Figure 9a. It is striking that when we plot the FOD distribution of nonhalo CMEs the "bump" at high distances decreases considerably, as shown in Figure 9b. The coefficients δ and ε are similar for both cases (total and nonhalo CMEs) as seen in columns 2 and 3 of Table 3.

[24] The trend of the FOD distribution for partial halo CMEs is opposite to the distribution for total CMEs, as shown in Figure 10a. The peak is at ~27 $R_\odot$ and decreases towards lower distances. In this case the distribution has an enhancement between 5 and 10 $R_\odot$, and then, does not fit very well the exponential law. On the other hand, the FOD distribution of full halo CMEs is very well fitted by the exponential model. It is clear from Figure 10b and Table 3 that the probability of a CME reaching large distances and

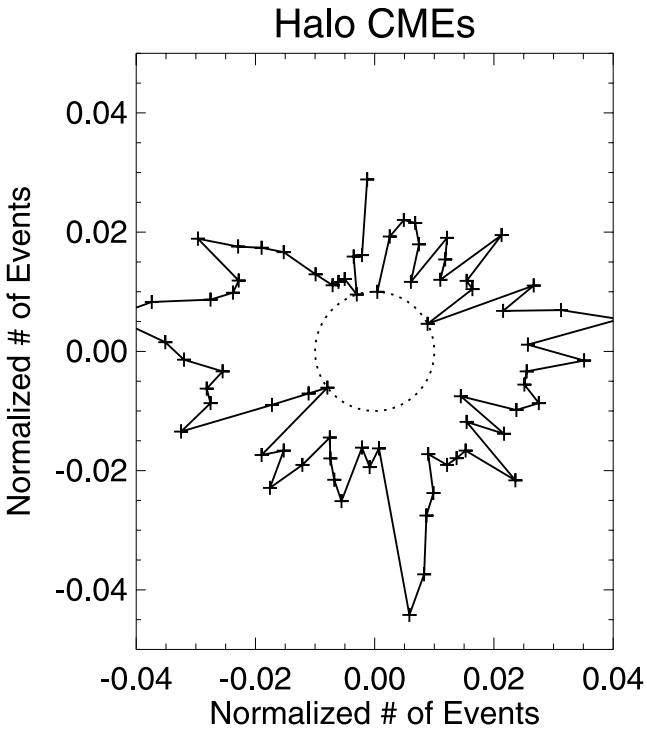

Figure 8. Full halo CME PA circular distribution, similar to Figure 7.

Table 2. Percentage of CMEs Divided by Quadrants

CME	Direction			
Halo	NE	SE	SW	NW
Nonhalo	23.7	23.8	26.7	25.7
Partial halo	23.3	25.3	27.5	23.8
Full halo	24.9	23.1	29.1	22.8

Table 3. Coefficients of FOD Models

	CME			
Coefficient	Total	Nonhalo	Partial Halo	Full Halo
δ	0.121	0.152	0.008	0.004
ϵ	−0.084	−0.099	0.083	0.114

be distinguishable from the background is higher for partial or full halo than for nonhalo CMEs.

3. Discussion

[25] It is clear from the analysis presented in previous sections that halo CMEs have a statistically different behavior compared to nonhalo CMEs. The current interpretation of halo CMEs as result of a geometrical effect, in which a regular CME is traveling toward (or away) the observer [*Gopalswamy*, 2004] is difficult to reconcile with the facts presented here. Then, it is necessary to look for an alternative model for halo CMEs.

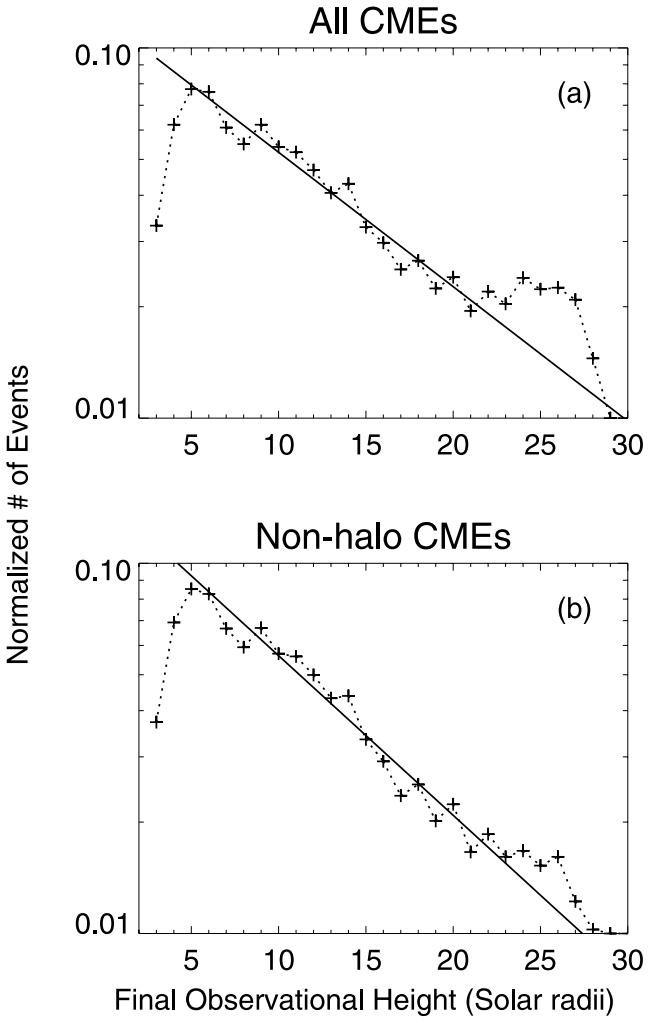

Figure 9. Final observed distance distribution for all observed (top) and nonhalo (bottom) CMEs, plus symbols represent the observed distributions with a bin size of 1 $R_\odot$. The continuous lines are the exponential models fitted to the points.

3.1. White Light CMEs

[26] White light CMEs are observed due to Thompson scattered photospheric light. The scattering theory of white light coronal structures was developed in the 1950s to analyze solar eclipse observations, and is discussed in detail by *Billings* [1966]. In terms of CMEs, the theory was reviewed by *Hundhausen* [1993] and more recently by *Andrews* [2002]. Basically, the observed (scattered) brightness, B_s, may be written as the integral along the line of sight, s, of the electronic density $N_e(s)$, and a function H which depends on (1) the photospheric flux $F(r, u)$, a function of the distance r from the photosphere to the scattering point and a limb darkening function u (which has not effect, $u \sim 1$, when $r > 2R_\odot$ [*Hundhausen*, 1993]); (2) the angle $\Omega(r)$ which is the angular solar radii, as seen at distance r (where the scattering center is located); and (3) the angle χ subtended between the Sun center-scattering point line and the observer-scattering point line (see *Billings* [1966] for details). This function may be written as:

$$B_s = \int N_e(s) H[F(r,u), \Omega(r), \chi] ds. \tag{8}$$

The observed brightness decreases with distance r (see Figure 3 of *Andrews* [2002]) and depends on $\sin(\chi)$, which is maximum when the Sun center-scattering point line is perpendicular to the observer-scattering point line (i.e., the scatter point lies in the plane of the sky) and is minimum when the scatter point is in the Sun-observer line [see *Andrews*, 2002, Figure 2].

[27] In the current interpretation of halo CMEs, they are traveling toward the observer, so that the angle χ tends to be in the Sun-observer direction. And at a fixed projected distance (from the center of the disk) the "true" Sun-scatter point distance is larger for a halo CME than that for a limb-CME. Thus in terms of the previous discussion of Thompson scattering theory, the final observed distance should be lower for full halo than for non-halo CMEs. This is in apparent contradiction with the observational findings discussed in section 2.6.

3.2. Alternative Explanation for Halo CMEs

[28] We suggest an alternative explanation for halo CMEs, which may explain the above discrepancy and all the characteristics discussed in previous sections: It is most likely that the halo seen in white light images is due to the density enhancement produced by a (shock) wave driven by a fast CME. In this case it is highly probable that the structures projected in the plane of the sky, observed by the coronographs, are a combination of the CME material plus

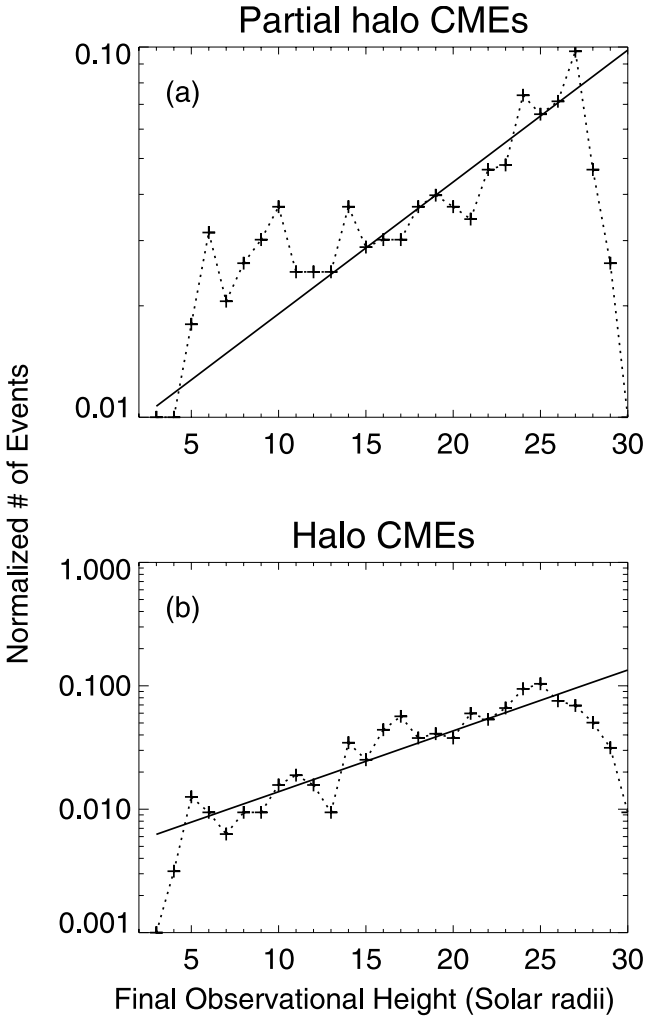

Figure 10. Final observed distance distributions for partial (top) and full (bottom) halo CMEs, similar to Figure 9.

the shock wave enhancement. As pointed out by *Sheeley et al.* [2000], the idea of shock waves originated at the Sun is not new. The problem is how to identify such waves. As we noted in the introduction, wide CMEs have been interpreted as a result of the deflection of coronal structures caused by the CME driven shock wave [Sime and *Hundhausen*, 1987; *Sheeley et al.*, 2000; *St. Cyr et al.*, 2005]. In this work we go further and consider not only the deflection of preexisting structures as a signature of the shock, but we speculate that the shock wave disturbs and compresses the ambient corona appearing as a wide (symmetric) brightness enhancement.

[29] The quiet Sun MHD fast mode speed has a peak value of ~540 km/s at ~3.5 $R_{\odot}$ [*Gopalswamy et al.*, 2001a]. Therefore any CME traveling at a higher speed is capable of driving a MHD shock. In principle, the pressure or density enhancements caused by these shocks can be observed in white light. However, it has been difficult to do so, since the observed features are projections in the plane of the sky of "all" the scattering electrons. In fact, the observed enhancement is the mixture of the background brightness, the CME, and (probably) the shock wave enhancements. Thus it is difficult to distinguish such structures in the present (one point) observations. Nevertheless, there are few cases of white light shock observations reported in the literature (see the discussion of *Sheeley et al.* [2000] and *Vourlidas et al.* [2003] about this subject). In particular, *Vourlidas et al.* [2003] used MHD simulations to support their interpretation of a white light faint halo surrounding a narrow CME as a shock wave.

[30] Shock waves have been invoked to explain expanding shells at newly formed stars [*Mac Low and Elitzur*, 1992; *Elitzur et al.*, 1989] as well as at late type stars [*Imai et al.*, 2003]. In the postshock region the enhancement of density and temperature is not as high as in the front but covers a considerable wider region for a longer time than the shock passage [*Hollenbach and McKee*, 1989]. This region has been found to be very rich in emission of different species of molecules in the interstellar medium and at stars. In particular the maser emission shows flux enhancements in regions that correspond to the postshock region [*Gwinn*, 1994; *Liljeström and Gwinn*, 2000]. Recently, *Ciaravella et al.* [2005] observed an extended region (~1 $R_{\odot}$) at a distance of 3.6 $R_{\odot}$, with a broad and blue-shifted component of the O_{VI} line. These authors interpreted this observation as a direct evidence of a CME driven shock and support the possibility of seeing these regions in white light coronograph images.

3.3. Type II Bursts and Halo CMEs

[31] It is well established that Type II bursts are the product of shock waves propagating outwards in the corona [*Nelson and Melrose*, 1985]. Therefore if halo features are the product of CME driven shocks in the corona, we may expect some relation between these two phenomena: Halo CMEs and type II burst. These relationship has been extensively studied [*Cliver et al.*, 1999; *Mann et al.*, 2003; *Lara et al.*, 2003; *Cliver et al.*, 2004; *Cane and Erickson*, 2005]. In particular, *Gopalswamy et al.* [2001b] found that only 40% of CMEs with speed higher than 900 km/s have an associated DH/km type II burst. They conclude that something more (than high speed) is needed for a CME in order to produce type II emission. In our case this percentage is equivalent to ~2.8% of the total number of CMEs.

[32] Unfortunately, we do not have spatial information of type II bursts, thus it is not possible to compare the type II and CME positions directly. Instead, we can use a coronal density model to associate a particular height to the type II disturbance and look for CMEs observed at this height around the same time. For example, the densities (n) involved in a type II burst observed at a fundamental frequencies (f) of 10 MHz and 4 MHz are 1.24×10^6 and 1.98×10^5 cm^{-3}, which, using *Leblanc et al.* [1998] coronal density model, are associated to heights of 2 and 3 $R_{\odot}$ (close to the lower CME eight observed by LASCO/C2).

[33] In order to test the possible relation between Type II bursts and halo CMEs and/or shock waves, we use the Type II bursts observed by Wind Waves experiment [*Bougeret et al.*, 1995] during the 1997–2004 period. From a total of 422 Type II bursts reported at http://lep694.gsfc.nasa.gov/waves/waves.html, 186 (262) have a starting frequency higher than 10 (4) MHz (or initial height lower than 2 (3) $R_{\odot}$). As a first approximation, we set a time window of 10 min before and after the reported Type II onset time and

Table 4. Number of Possible CME-Type II Burst Associated Events

CME	Number of Type II Bursts			
	10 MHz		4 MHz	
Halo	Before	After	Before	After
Nonhalo	5	8	5	9
Partial halo	5	12	8	15
Full halo	19	15	25	16

checked for CMEs with (LASCO/C2) first observation times inside such time windows. Table 4 shows the number of possible CME-Type II association, where the labels mean that the CME LASCO/C2 first observation time is before (columns 2 and 4) and after (columns 3 and 5) the reported Type II onset time. It is interesting that ~27% of the high-frequency (10 MHz) events may be related to a (partial or full) halo CME, whereas only ~7% is related to nonhalo CMEs. At a lower-frequency (4 MHz), ~24% are related to halo and ~5% to nonhalo CMEs. It is necessary to perform a deeper analysis about the Type II and halo CME pair association, but this preliminary analysis shows that if there is a CME observed at 2–3 $R_\odot$ around the starting time of a coronal type II, it is more likely that this is a partial or full halo than a nonhalo CME.

3.4. Halo CME Scenario

[34] As a possible scenario of what we are seeing when a halo CME takes place, in the first and third columns of Figure 11 we show a series of difference images from LASCO/C3 of the CME observed on April first, 2000, and reported as a white light shock wave candidate by *Vourlidas et al.* [2003]. A C2.6 flare starting at 1938 UT was reported at N26E30 position. This position is not consistent with the CME PA angle which is reported as 291° in the CME catalog (http://cdaw.gsfc.nasa.gov). This CME was first seen at 1954 UT by LASCO/C2 with an angular width of 33° and relatively low (projected) speed of

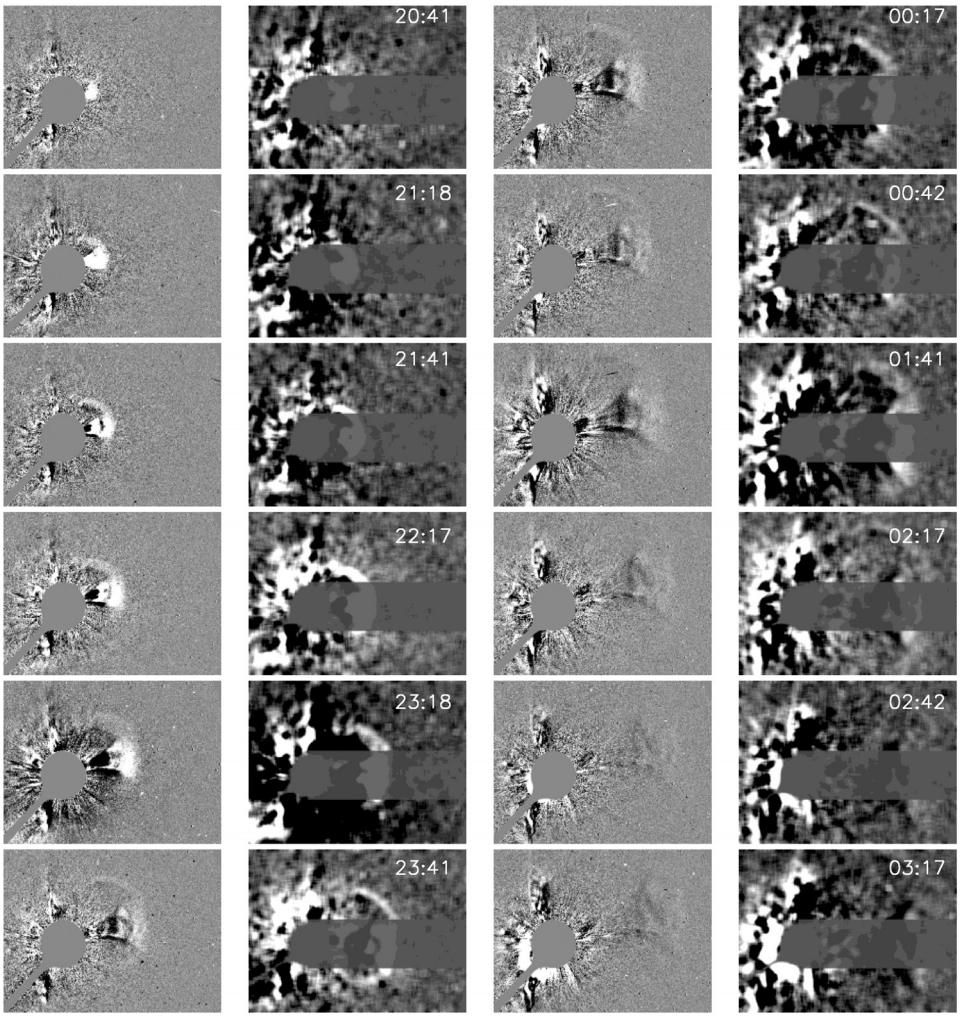

Figure 11. Possible shock wave observed during the 1 April 2000 CME by LASCO. The first and third columns is the CME sequence; the second and fourth columns is the corresponding sequence but enhanced and rotated 15° clockwise, in such a way that an observer situated on the west limb direction, will see a full halo CME coming from the center of the disk. The dark shadow area represents the occulter disk as seen by this observer.

586 km/s. Extreme Ultraviolet Imaging Telescope (EIT) [*Delaboudiniere et al.*, 1995] 195 images show a dimming (activity related to CMEs [*Thompson et al.*, 2000]) followed by a loop brightening starting at ~1936 UT and close to the west limb (~N05W43). This activity is most likely to be associated with the CME. Thus this CME may be considered as a near limb CME.

[35] If we rotate the LASCO images by 15° clockwise, the new rotated CME PA is ~270, so this will be a CME traveling close to the ecliptic plane toward the west direction. In this way, an observer situated in this direction will detect something like the images on the second and fourth columns of Figure 11, where we show the same LASCO/C3 images (of the first and third column) but rotated and enhanced to see better the CME and (probable shock) wave brightenings. To give a better idea of what the observer in the far west side will see, we extended the occulter shadow, toward the west limb, so the shaded portion of the CME will be "invisible" to that observer.

[36] It is interesting to note the long integration distance along the line of sight of the west observer when he is seeing the flanks of the (probable shock) wave. This observer will see a wide bright CME. We note also that the projected CME speed is marginally higher than the (MHD) fast mode speed at 5 $R_\odot$ but is almost double at $10_\odot$ [see *Gopalswamy et al.*, 2001a, Figure 3], i.e., this speed is high enough to form a shock wave.

4. Conclusion

[37] Through a statistical analysis of the parameters of 9224 coronal mass ejections observed by LASCO/SOHO during the 1996–2004 period, we found:

[38] 1. Width: The CME width distribution is multimodal, thus it can be divided in width intervals where different modes fit well: (1) narrow $W_N < 25°$ and medium width $30° < W_M < 80°$ CMEs are fitted by a gaussian model, with a mean value of 16.8° and 37.6°, respectively. (2) For CMEs with $80° < W_L < 210°$, the distribution follows an exponential law. (3) The wide CMEs $W_W > 210°$ are clearly out of the power law and do not seems to follow any particular distribution. We found that the narrow part of the width distribution is due to "true" widths, whereas the medium width part of the distribution is the result of the projection effects.

[39] 2. Number of halo CMEs: Taking into account geometrical effects only, the number of observed full halo CMEs is lower than expected.

[40] 3. Speed: The CME speed distribution is of the log-normal type, even though it shows that there is a low speed ($v < 100$ km/s) gaussian "bump" which may be related to projection effects. The speed distributions peak at 303, 392 and 615 km/s for nonhalo, partial halo, and full halo CMEs, respectively.

[41] 4. Acceleration: The acceleration distribution does not follow any standard function. More than 50% of full halo CMEs have negative acceleration, whereas only ~35% of nonhalo and partial halos have negative acceleration.

[42] 5. Position Angle: CMEs are lunched preferentially in the active region belt. There is a small east-west asymmetry with a ~2% excess of events in the western hemisphere.

[43] 6. Final Observed Distance: The distribution of the final observed distance, defined as the distance from the center of the disk, where the CME brightness enhancement reaches the background level, and is "lost" by the observer, follows an exponential law. As expected, the exponential index is negative for non-halo CMEs (~−0.1), i.e., fewer CMEs can be followed up to higher distances in the coronograph field of view. However, the exponential index changes completely (~0.1) for full halo CMEs, meaning that full halo are observable at larger distances than nonhalo CMEs.

[44] From the above facts, we conclude that halo CMEs cannot be explained merely as a geometrical effect, i.e., regular CMEs traveling in the Sun-Earth direction. As an alternative, we propose that the observed "halo" is the manifestation (compressed material) of the (shock) wave driven by fast CMEs. If this is the case, then (1) the halo must be wide and does not have to follow the CME width distribution. (2)The number of halos is determined by the CME direction (close, but not necessarily in the Sun-Earth direction) and (3) CME speed which should be higher than the fast magnetosonic mode speed of the coronal background. (4) Fast CMEs form a shock wave and lose momentum showing deceleration. (5) In contrast with the driving CME, which is traveling fast at ~90° out of the plane of the sky, the shock wave may be extended "backward" toward the plane of the sky and thus have better conditions to be detected through Thompson scattering effect. In this way, halos may be seen at larger projected distances.

[45] As the relationship between shock wave and type II bursts in the decametric-hectometric range is well known, we examined the relationship between halo CMEs and Type II bursts. In this preliminary analysis, we restrict our study to type II bursts starting at frequencies lower than 10 and 4 MHz and set a time window of 10 min before and after the reported type II onset time. We found that 27% and 24% of high (10 MHz) and low (4MHz) frequency events are related to a partial or full halo, and only 7% and 5% are related to nonhalo CMEs.

[46] The evidences presented in this work show that halo CMEs cannot be purely "regular" CMEs traveling in the Sun-Earth direction. A conclusive study is necessary, but the evidences presented here suggest the possibility that the observed halos are the combination of the enhancement due to a shock wave driven by a fast CME and the CME material.

[47] **Acknowledgments.** We are grateful with the reviewers for their constructive comments. Thanks to Seiji Yashiro for the CME data. This work was partially supported by UNAM grant PAPIIT-IN119402 and CONACyT.

[48] Shadia Rifai Habbal thanks Yong-Jae Moon and E. W. Cliver for their assistance in evaluating this paper.

References

Andrews, M. D. (2002), The front-to-back asymmetry of coronal emission, *Sol. Phys.*, *208*, 317–324.

Billings, D. E. (1966), *A Guide to the Solar Corona*, Elsevier, New York.

Bougeret, J.-L., et al. (1995), WAVES: The Radio and Plasma Wave Investigation on the WIND spacecraft, *Space Sci. Rev.*, *71*, 5.

Brueckner, G. E., et al. (1995), The Large Angle and Spectrometric Coronagraph (LASCO), *Sol. Phys.*, *162*, 357–402.

Cane, H. V., and W. C. Erickson (2005), Solar type II radio bursts and IP type II events, *Astrophys. J.*, *623*, 1180–1194.

Ciaravella, A., J. C. Raymond, S. W. Kahler, A. Vourlidas, and J. Li (2005), Detection and diagnostics of a coronal shock wave driven by a partial halo coronal mass ejection on 2000 June 28, *Astrophys. J.*, *621*, 1121–1128.

Cliver, E. W., D. F. Webb, and R. A. Howard (1999), On the origin of solar metric type II bursts, *Sol. Phys.*, *187*, 89–114.

Cliver, E. W., N. V. Nitta, B. J. Thompson, and J. Zhang (2004), Coronal shocks of November 1997 revisited: The CME type II timing problem, *Sol. Phys.*, *225*, 105–139.

Crifo, F., J. P. Picat, and M. Cailloux (1983), Coronal transients—Loop or bubble, *Sol. Phys.*, *83*, 143–152.

Delaboudiniere, J.-P., et al. (1995), EIT: Extreme-Ultraviolet Imaging Telescope for the SOHO mission, *Sol. Phys.*, *162*, 291–312.

Elitzur, M., D. J. Hollenbach, and C. F. McKee (1989), H2O masers in star-forming regions, *Astrophys. J.*, *346*, 983–990.

Gopalswamy, N. (2004), A global picture of CMEs in the inner heliosphere, in *The Sun and the Heliosphere as an Integrated System*, *ASSL Ser.*, edited by G. Poletto and S. Suess, p. 201, chap. 8, Springer, New York.

Gopalswamy, N., A. Lara, M. L. Kaiser, and J.-L. Bougeret (2001a), Near-Sun and near-Earth manifestations of solar eruptions, *J. Geophys. Res.*, *106*, 25,261.

Gopalswamy, N., S. Yashiro, M. L. Kaiser, R. A. Howard, and J.-L. Bougeret (2001b), Characteristics of coronal mass ejections associated with long wavelength type II radio bursts, *J. Geophys. Res.*, *29*, 219.

Gwinn, C. R. (1994), Hypersonic acceleration and turbulence of H2O masers in W49N, *Astrophys. J.*, *429*, 241–252.

Hollenbach, D., and C. F. McKee (1989), Molecule formation and infrared emission in fast interstellar shocks. III - Results for J shocks in molecular clouds, *Astrophys. J.*, *342*, 306–336.

Howard, R. A., D. J. Michels, N. R. Sheeley Jr., and M. J. Koomen (1982), The observation of a coronal transient directed at earth, *Astrophys. J.*, *263*, L101–L104.

Howard, R. A., N. R. Sheeley Jr., D. J. Michels, and M. J. Koomen (1985), Coronal mass ejections - 1979–1981, *J. Geophys. Res.*, *90*, 8173–8191.

Hundhausen, A. J. (1987), The origin and propagation of coronal mass ejections, in *Proceedings of the Sixth International Solar Wind Conference*, edited by V. J. Pizzo, T. Holzer, and D. G. Sime, *Tech. Note NCAR/TN-306+Proc*, p. 181, Natl. Cent. for Amtos. Res., Boulder, Colo.

Hundhausen, A. J. (1993), Sizes and locations of coronal mass ejections: SMM observations from 1980 and 1984–1989, *J. Geophys. Res.*, *98*, 13,177–13,200.

Imai, H., K. M. Shibata, K. B. Marvel, P. J. Diamond, T. Sasao, M. Miyoshi, M. Inoue, V. Migenes, and Y. Murata (2003), The three-dimensional kinematics of water masers around the semiregular variable RT Virginis, *Astrophys. J.*, *590*, 460–472.

Lara, A., N. Gopalswamy, S. Nunes, G. Muoz, and S. Yashiro (2003), A statistical study of CMEs associated with metric type II bursts, *Geophys. Res. Lett.*, *30*(12), 8016, doi:10.1029/2002GL016481.

Leblanc, Y., G. A. Dulk, and J.-L. Bougeret (1998), Tracing the electron density from the corona to 1 AU, *Sol. Phys.*, *183*(1), 165–180.

Liljeström, T., and C. R. Gwinn (2000), Water masers diagnosing post-shocked conditions in W49N, *Astrophys. J.*, *534*, 781–800.

Mac Low, M. M., and M. Elitzur (1992), Water masers in W49N: The youngest stellar jet?, *Astrophys. J.*, *393*, L33–L36.

Mann, G., A. Klassen, H. Aurass, and H.-T. Classen (2003), Formation and development of shock waves in the solar corona and the near-Sun interplanetary space, *Astron. Astrophys.*, *400*, 329–336.

Nelson, G. J., and D. B. Melrose (1985), Type II bursts, in *Solar Radiophysics: Studies of Emission from the Sun at Metre Wavelengths*, pp. 333–359, Cambridge Univ. Press, New York.

Sheeley, N. R., J. H. Walters, Y.-M. Wang, and R. A. Howard (1999), Continuous tracking of coronal outflows: Two kinds of coronal mass ejections, *J. Geophys. Res.*, *104*, 24,739–24,768.

Sheeley, N. R., W. N. Hakala, and Y.-M. Wang (2000), Detection of coronal mass ejection associated shock waves in the outer corona, *J. Geophys. Res.*, *105*, 5081–5092.

Sime, D. G., and A. J. Hundhausen (1987), The coronal mass ejection of July 6, 1980: A candidate for interpretation as a coronal shock wave, *J. Geophys. Res.*, *92*, 1049–1055.

St. Cyr, O. C., et al. (2000), Properties of coronal mass ejections: SOHO LASCO observations from January 1996 to June 1998, *J. Geophys. Res.*, *105*, 18,169–18,185.

St. Cyr, O. C., et al. (2005), The last word: The definition of halo coronal mass ejections, *Eos Trans. AGU*, *86*(30), 281–282.

Thompson, B. J., E. W. Cliver, N. Nitta, C. Delanné, and J.-P. Delaboudinière (2000), Coronal dimmings and energetic CMEs in April–May 1998, *Geophys. Res. Lett.*, *27*, 1431–1434.

Trottet, G., and R. M. MacQueen (1980), The orientation of pre-transient coronal magnetic fields, *Sol. Phys.*, *68*, 177–186.

Vourlidas, A., S. T. Wu, A. H. Wang, P. Subramanian, and R. A. Howard (2003), Direct detection of a coronal mass ejection-associated shock in large angle and spectrometric coronagraph experiment white-light images, *Astrophys. J.*, *598*, 1392–1402.

Wang, Y. M., P. Z. Ye, S. Wang, G. P. Zhou, and J. X. Wang (2002), A statistical study on the geoeffectiveness of Earth-directed coronal mass ejections from March 1997 to December 2000, *J. Geophys. Res.*, *107*(A11), 1340, doi:10.1029/2002JA009244.

Webb, D. F., and R. A. Howard (1994), The solar cycle variation of coronal mass ejections and the solar wind mass flux, *J. Geophys. Res.*, *99*, 4201–4220.

Xie, H., L. Ofman, and G. Lawrence (2004), Cone model for halo CMEs: Application to space weather forecasting, *J. Geophys. Res.*, *109*, A03109, doi:10.1029/2003JA010226.

Yashiro, S., N. Gopalswamy, G. Michalek, O. C. St. Cyr, S. P. Plunkett, N. B. Rich, and R. A. Howard (2004), A catalog of white light coronal mass ejections observed by the SOHO spacecraft, *J. Geophys. Res.*, *109*, A07105, doi:10.1029/2003JA010282.

Zhang, J., K. P. Dere, R. A. Howard, and V. Bothmer (2003), Identification of solar sources of major geomagnetic storms between 1996 and 2000, *Astrophys. J.*, *582*, 520–533.

N. Gopalswamy, NASA Goddard Space Flight Center, Greenbelt, MD 20771, USA.

A. Lara, Instituto de Geofísica, UNAM, C. U. México D. F. 04510, México. (alara@geofisica.unam.mx)

E. Mendoza-Torres, Instituto Nacional De Astrofísica Óptica y Electrónica, Tonantzintla 72840, México.

G. Michalek, Astronomical Observatory of Jagiellonian University, Krakow 30-244, Poland.

R. Pérez-Eríquez, Centro de Geociencias, Universidad Nacional Autónoma de México, Querétaro 76001, México.

H. Xie, Catholic University of America, 620 Michigan Avenue NE, Washington, DC 20064, USA.